Geophys. J. Int. (2007) **168,** 583–592 doi: 10.1111/j.1365-246X.2006.03055.x

Velocity images from stacking depth-slowness seismic wavefields

Geraint D. Jones,[1,*] Penny J. Barton[1] and Satish C. Singh[2]

[1] *Bullard Laboratories, University of Cambridge, Madingley Road, Cambridge* CB3 0EZ, *UK*
[2] *Laboratoire de Geosciences Marines, IPG Paris, France*

Accepted 2006 April 27. Received 2006 April 26; in original form 2005 September 9

SUMMARY

We present synthetic and real data examples processed using a depth imaging method for long-offset multichannel seismic data via the intercept-time-slowness (τ–p) domain. The refracted and reflected information contained in the wavefield is processed simultaneously. Our scheme uses common midpoint data that is transformed to the τ–p domain and mapped to the depth-slowness (z–p) domain using a downward continuation algorithm. The velocity function for downward continuation may be obtained iteratively from the diving ray trajectory within the slowness-depth wavefield or estimated using an independent method. Horizontal events within the z–p wavefield are isolated by applying a mute function corresponding to the downward continuation velocity function in the z–p domain. Stacking the resulting wavefield gives an image trace that may be superimposed on the velocity function to form a velocity image. Following testing on synthetic data the method is applied to two long-offset marine seismic streamer data sets with offsets up to 18 km, from the northeast Atlantic margin. These examples demonstrate the potential of the method to obtain velocity images in difficult geological locations, where conventional processing has been less successful.

Key words: depth-slowness, downward continuation, intercept time, slowness, tau, velocity image.

1 INTRODUCTION

Marine multichannel seismic surveys have been recorded with offsets up to 30 km, by using multiple passes with two ships in a synthetic aperture configuration (Buhl *et al.* 1982). Such surveys have been particularly popular in areas where sub-basalt imaging has been a problem, as the high impedance contrast between the basalt and the surrounding sedimentary rocks seriously hinders the transmission of seismic energy and, therefore, degrades the quality of seismic images beneath both intruded and extruded basalt structures. These basaltic structures can also be extremely heterogeneous in nature. In the case of extruded basalts there may be a high degree of rugosity at the top and base of each individual flow, or a layer several kilometres thick may be composed of a series of individual flows giving rise to an internally layered structure that may be interbedded with sedimentary horizons. In the case of igneous intrusions a complex pattern of sills and dykes may form as they are intruded along lines of weakness in the country rock. In both the intruded and extruded case the heterogeneity leads to a high degree of scattering as the seismic wave passes through a basalt structure, preferentially attenuating the high-frequency components (Hobbs 2002). Contamination from multiple arrivals may also be a serious problem.

These new data sets contain arrival phases from reflections and refractions in the sub-surface, densely sampled from near normal incidence to post-critical offsets. Conventionally the near offset information is processed with commercially available software. The end product of this processing is usually a stacked section (image) in time or depth from which details of structures in the sub-surface may be inferred. Long-offset data, which consists of refractions and post-critical reflections, may be degraded by the application of near offset processing methods, particularly normal moveout stretch, (Shah & Levin 1973) and instead are often analysed with traveltime techniques such as modelling and first break tomographic inversion. The result of the traveltime approach is a velocity model of the sub-surface from which it may be possible to interpret changes in lithology (Zelt & Smith 1992). If data using near and far offset acquisition methods are collected in the same place, the results from the two processing approaches are frequently overlaid as a final stage to provide a velocity-mapped image of the sub-surface (e.g. Hughes *et al.* 1997), but none of these existing techniques is optimized for analysing the reflected and refracted components of the wavefield simultaneously.

There is a need for a new type of processing strategy that can be applied to these new data sets in an integrated way. Transforming the data from the t–x domain to the τ–p (intercept time, horizontal

*Now at: Offshore Hydrocarbon Mapping Ltd, The Technology Centre, Claymore Drive, Aberdeen, AB23 8GD, UK. E-mail: geraint.jones@ohmsurveys.com

slowness) domain has proved beneficial in separating the wavefield into reflection and refraction components (Chapman 1981; Diebold & Stoffa 1981). Clayton & McMechan (1981) demonstrated how it was possible to map the *t–x* domain data to the depth-slowness (*z–p*) domain via the τ–p transform using a downward continuation algorithm. Their work used refraction data to obtain a *z–p* image corresponding to the velocity function for a single gather. In Jones *et al.* (2003) we introduced a new method that built on the work of Clayton & McMechan (1981) in the τ–p domain, by using the velocity function extracted during downward continuation as a mute, and stacking the remaining flattened reflected energy to create an image trace in depth for each common midpoint (CMP). Here we test and illustrate this method with synthetic and real data examples, and compare our results with conventional stacks and with the results from waveform inversion. We also evaluate the contribution of the longer-offset data to the image, and demonstrate that the full range of offset has indeed been exploited effectively. Our examples show that the method produces useful images of sub-basalt structure in an area of the northeast Atlantic margin that has proved difficult to image using conventional techniques.

2 THE τ–P TRANSFORM AND DOWNWARD CONTINUATION

The first processing applications of the τ–p transform used a simple linear slant stack (Schultz & Claerbout 1978), defined as

$$f(\tau, p) = \int_0^\infty F(\tau + px, x)\, dx, \tag{1}$$

where F and f are the observed and transformed wavefields, respectively, and

$$t = \tau + px, \tag{2}$$

where

$$p = \frac{dt}{dx}. \tag{3}$$

Using eq. (1), head wave refractions and reflections in the *t–x* domain transform to points and ellipses, respectively, in the τ–p domain. Diving waves, associated with velocity gradients in the sub-surface, transform to high-amplitude arrivals in the τ–p domain that link the high-slowness upwardly concave ends of the reflection ellipses with short upwardly convex segments (see Fig. 2b). The τ–p wavefield may be mapped to the depth-slowness (*z–p*) domain using a downward continuation algorithm (Clayton & McMechan 1981; Jones *et al.* 2003) and a velocity-depth function. The operator Ψ, used to perform the downward continuation to depth z has the form

$$\Psi(p, z) = \int_0^z (u(z)^2 - p^2)^{1/2}\, dz, \tag{4}$$

where $u(z)$ is an estimate of the velocity-depth function.

If downward continuation has been performed with the correct velocity function, and anisotropy is negligible, the τ–p reflection ellipses will become flattened to horizontal events in the *z–p* domain. The high-amplitude diving ray trajectory on the τ–p plot corresponds to the required background velocity function for downward continuation. This velocity function may be extracted automatically from the data using an iterative process described in Clayton & McMechan (1981). Before the horizontal events are stacked to construct the final image trace, a mute function must be applied to the *z–p* wavefield to prevent the high-amplitude stretched traces of the background velocity function dominating the final trace. The mute function is based simply on the integrated velocity function over depth (eq. 4).

Once the mute function has been applied the horizontal events in the τ–p wavefield are isolated. The final stage of the processing is to stack the flattened reflection events to enhance coherency, to reduce the effect of random noise and to eliminate events that are not primary reflections. To calculate the number of traces to stack into the final image we assume that $u(z)$ is equal to $p_{\max}(z)$ for turning rays and critical angle reflections. The integer number of traces N, is then

$$INT\left[\frac{p_{\max}(z)}{dp}\right] = N, \tag{5}$$

where dp is the slowness increment. The final image $I(z)$ at any given depth within the wavefield $S(p_j, z)$ is given by

$$I(z) = \frac{1}{N}\sum_{j=1}^{N} S(p_j, z). \tag{6}$$

The stacked image trace may be readily displayed overlying the corresponding velocity function allowing structural changes to be correlated directly with velocity changes. Because some multiple energy survives the transform to τ–p and appears in the part of the data we wish to stack, multiple attenuation forms a crucial preprocessing step prior to downward continuation.

3 SYNTHETIC DATA

We tested the scheme by applying it to synthetic data from a simple plane-layered model. These tests aid in understanding the processing method as individual events may be tracked through each stage of the process from the $x - t$ gather to the final image trace.

Diebold & Stoffa (1981) analysed various acquisition geometries for the application of the τ–p transform, and they demonstrate the advantage of the CMP domain for the transformation of data in the presence of dip angles up to 5°, due to the averaging of vertical slownesses from up and downgoing wavefields; therefore, the CMP domain was chosen here.

A simple model was constructed consisting of horizontal layers with vertical velocity gradients (Fig. 1a). An acoustic finite difference algorithm was used to generate a synthetic CMP gather with a maximum offset of 20 km and a trace spacing of 12.5 m (Fig. 1b). Two offset ranges were chosen in order to investigate the contribution of the longer offset data to the final image: 0–3 km and 0–20 km. An offset range of 0–3 km approximately represents a 'standard' marine acquisition streamer length, while an offset range of 0–20 km is achievable using two vessels and long streamers in a synthetic aperture configuration (Buhl *et al.* 1982).

The τ–p transforms of the first 3 km offset of data and the entire 20 km offset are shown in Fig. 2. There are two distinct effects of including the long-offset information in the transform. Firstly the diving ray events seen on the 20 km offset τ–p gather (Fig. 2b), are not present on the 3 km offset transform (Fig. 2a). Secondly the τ–p reflection ellipses from the 3 km offset data are incomplete (Fig. 2a). Using the full range of offsets in the τ–p transform results in an extension of the τ–p reflection ellipses from low towards intermediate values of slowness, particularly for the deeper events (Fig. 2b). This extension results from coherent energy being recorded from a wider range of p values in the long-offset CMP gather than in the 3 km offset gather. The τ–p transform has generated some artefacts visible in Fig. 2 that have been mapped to depth in Fig. 3. These artefacts may

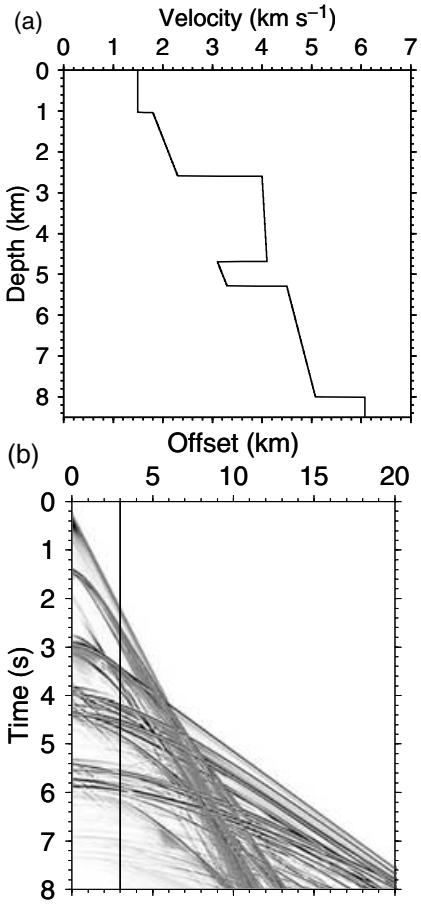

Figure 1. (a) 1-D velocity model consisting of a water column above an upper layer with a strong velocity gradient (sediments). Beneath this is a high-velocity unit representing a basalt layer, and a low-velocity zone between the basalt and the basement at 5.4 km depth. This velocity structure is representative of a continental margin setting from the northeast Atlantic. (b) Synthetic CMP gather produced from the velocity model in (a). The refracted diving ray may be seen as the first arrival beyond 6 km. The vertical line positioned at 3 km offset corresponds to the length of a 'standard' streamer.

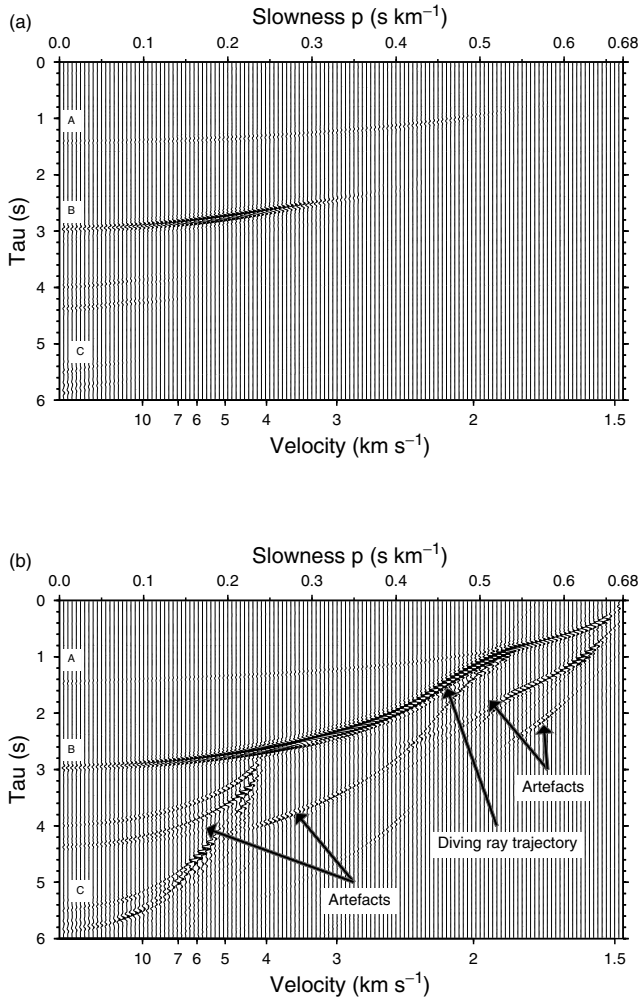

Figure 2. τ–p transform of the CMP gather in Fig. 1(b). (a) First 3 km of offset, and (b) full 20 km offset. The diving wave trajectory and the extension of the reflection ellipses corresponding to A (seafloor), B (top basalt layer interface) and C (deep interfaces, see also Fig. 1) is visible only in (b). (Artefacts generated during the τ–p transformation are visible on the right hand side of the τ–p wavefield obtained from the full offset gather (Fig. 2b). However, they are well away from the diving rays and will not require removal prior to continued processing.)

have been generated during the finite difference algorithm required to transform the wavefield.

The short and long offset τ–p wavefields were downward continued to a depth of 8.5 km (Figs 3a and b) using the correct velocity model (Fig. 1(a)) as described in Section 2. Downward continuation with the correct velocity model results in the reflection ellipses becoming flattened at a depth corresponding to the position of the layer interfaces in the model used to generate the data. The signal from the events at 4.8, 5.5 and 8.2 km depth were considerably enhanced in the z–p wavefield as a result of using the entire offset (compare Figs 3a and b). The velocity model (Fig. 1a) converted to z–p is shown superimposed on the z–p wavefield as an aid to identifying the background velocity trajectory. The horizontal events in the z–p wavefield correspond to the velocity discontinuities in the model.

Fig. 3 also illustrates how the high-amplitude diving wave events are mapped from the τ–p domain to the z–p domain. These events describe the trajectory of the background velocity in the τ–p domain. The strongest amplitudes are confined to the upper layer (1.1–2.6 km depth), where the velocity gradient is steep. At depth the diving rays are far less prominent as a result of the reduced velocity gradient in the second layer of the model (2.6–4.8 km depth), which lowers their amplitude and increases their slope. The low-velocity zone at 4.8–5.2 km depth creates a gap in the transformed data demonstrating the difficulty of using a completely automated method to determine the velocity function. As Fig. 3 shows, the velocity function p value at the top of the low-velocity layer at 4.8 km depth (Z') does not correspond to any feature in the z–p wavefield, and constraining the velocity in the low-velocity zone is problematic.

The final image trace is formed after applying a mute function to the z–p wavefield (Fig. 4). The mute is defined by the downward continuation velocity function, bulk shifted slightly (here by 0.05 s km^{-1}) towards lower slowness to eliminate stretched waveforms corresponding to the high-amplitude diving waves falling along the velocity function trajectory. The remaining horizontal events may be stacked to form the final image trace for a particular CMP supergather location. The final image traces for the two wavefields of Fig. 3 (3 and 20 km maximum offsets) are displayed in Fig. 5. Both traces have similar amplitudes for the events at 1.0 km

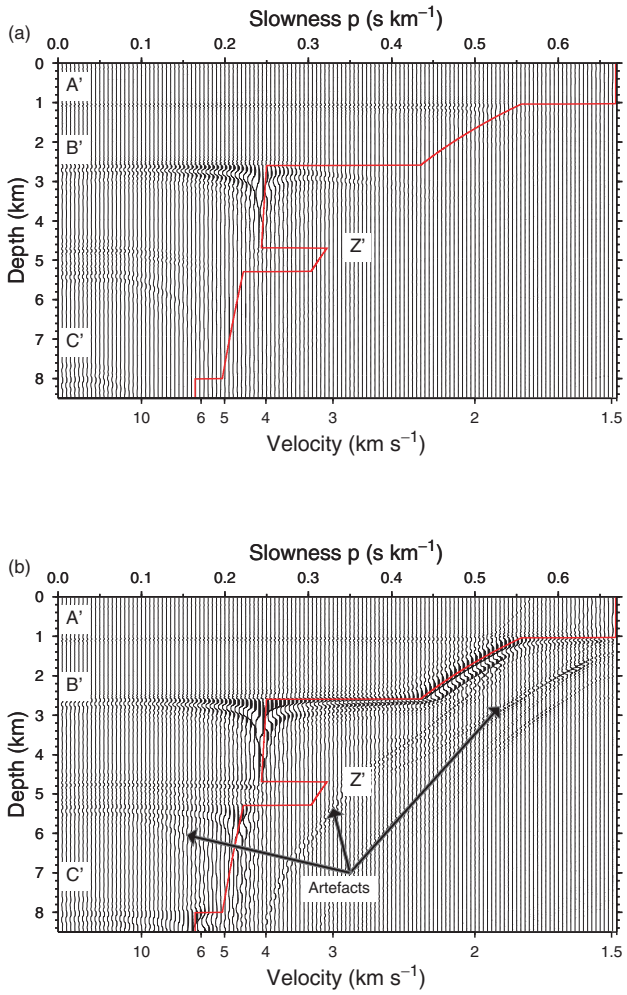

Figure 3. Depth-slowness (z–p) wavefield after downward continuation with the correct velocity function (Fig. 1a), converted to z–p, shown in red. (a) First 3 km of offset and (b) full 20 km offset. Using the correct velocity function in the downward continuation results in the mapping of the τ–p reflection ellipses to horizontal events. The seafloor event (A'), the first interface (B') and the deeper interfaces (C') are labelled. In (b), note the correlation of the diving ray trajectory with the locus of maximum amplitude of the 20 km offset wavefield. The top of the low-velocity zone (Z') does not correspond with any obvious feature at intermediate slowness in the z–p wavefield. (Artefacts are also mapped from the τ–p domain to z–p, some coinciding with the flattened reflection ellipses at 4.8, 5.5 and 8.2 km depth).

(seafloor, A') and 2.5 km (first interface, B', corresponding to top basalt) depth. However, at deeper levels the 20 km offset image trace has considerably enhanced amplitudes corresponding to the model interfaces at 4.8, 5.2 and 8.0 km depth (C', top basement) compared with the image trace formed only from the near offset information.

This demonstration shows how, for a 1-D model, enhanced images may be obtained from beneath a high impedance layer such as basalt by the inclusion of long-offset information into the stack.

4 APPLICATION TO DATA FROM THE NORTHEAST ATLANTIC MARGIN

4.1 Example 1: Thick continuous basalt flows

A long-offset multichannel seismic data set was acquired in the Faeroe–Shetland Basin by Veritas DGC Ltd in 1998 as part of a larger

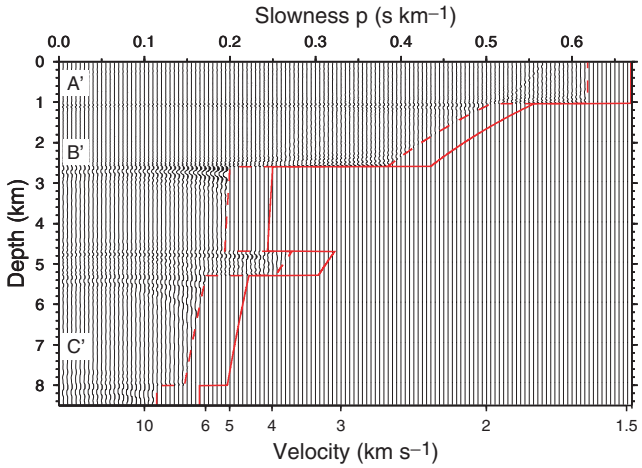

Figure 4. 0–20 km offset z–p wavefield from Fig. 3(b) after application of the mute function. The velocity function (solid red line) defines the mute function. This function is bulk shifted to lower values of p by about 0.05 s km^{-1} (dashed red line) to prevent the inclusion of the stretched high-amplitude diving ray trajectory events. Events A' (seafloor), B' (first interface) and C' (deep interface) are labelled as before.

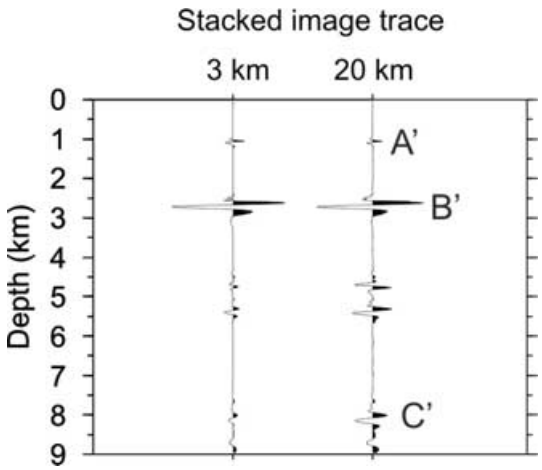

Figure 5. The image traces of the 0–3 and 0–20 km offset wavefields shown in Fig. 3 after application of the velocity function as a mute (see Fig. 4) and stacking. The seafloor (A': 1.0 km depth) and first reflector (B': 2.5 km depth) have similar amplitudes on both traces (amplitudes are directly comparable because the same velocity function was used to form both image traces). However, at depth the inclusion of the wide-angle data within the 20 km offset gather has significantly enhanced the image of the events at 4.8 km (base basalt), 5.4 km (top basement) and 8 km (C': deep interface) depth compared with using only the near offset traces.

regional investigation in which the long-offset events were to be used to aid in imaging beneath an extensive basalt layer. The Faeroe–Shetland Basin is a region of frontier exploration on the northeast Atlantic margin where potential hydrocarbon bearing sediments are thought to underlie parts of the basalt covering. The survey used a two-ship acquisition geometry to produce an extended long-offset data set with almost continuous sampling at an interval of 25 m up to nearly 18 km offset. The lead ship towed a 12 km streamer and the tail of this streamer was followed at approximately 1 km distance by a second vessel towing a 5 km streamer. Shots were fired every 75 m by the leading vessel.

Short portions of the data were selected for detailed investigation, and different approaches have already been presented by Carpenter

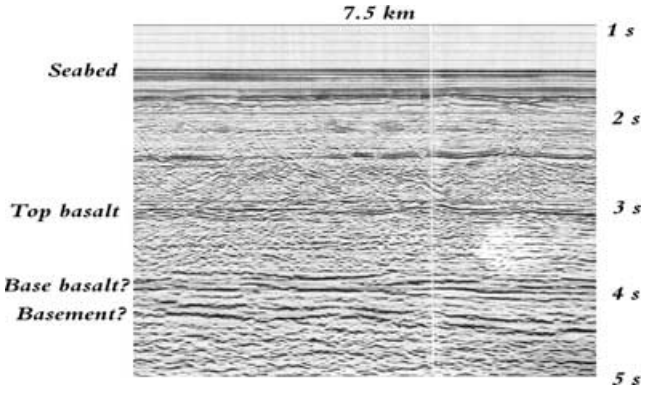

Figure 6. A stacked section of the Veritas processed Faeroes–Shetland data with a basic interpretation of the main structural horizons, after Shipp & Singh (2002).

(2001), who adopted a processing strategy and Shipp & Singh (2002) who applied traveltime tomography and 2-D full waveform inversion to investigate the data. In Jones *et al.* (2003) we showed a stack of one section of the data using the τ–p stacking method presented here and we also showed a stack of a second portion of data, using a velocity model obtained from traveltime modelling of refracted data by Shipp & Singh (2002). Here we revisit the second section of data and downward continue using a velocity function extracted from the data, before comparing and correlating the resulting image with the waveform inversion results from the same data.

In addition to the raw data, Veritas provided paper copies of stacked time sections produced by processing the first 6 km of offset. An image of part of one of these sections corresponding to the data presented here is shown in Fig. 6. A characteristic of the data from this region are multiples generated by the seafloor at about 1.5 s two-way time: the first of these is coincident with the top basalt reflection at near offsets. Veritas tackled this problem using multiple suppression techniques to enhance the weaker events below the basalt layer.

In Fig. 6 it is evident that the structure across this part of the line is quite stratified. The gently dipping seafloor reflector corresponds to water depths of 1.0–1.11 km, assuming a constant sea-water velocity of 1.48 km s^{-1}. A strong sedimentary reflection arrives at about 1.7–1.8 s, shallowing slightly towards the right hand end of the section. The next major reflection horizon at 2.5 s appears discontinuous. The top basalt reflection occurs at 3.1 s and appears fragmented in nature, also following the upward-dipping trend of the sedimentary horizons at the right hand end of the profile. At approximately 4 s, a series of coherent events across the section are interpreted as the base of the basalt layer. A deeper undulating and discontinuous event varying in arrival time from 4.1–4.3 s is assumed to mark the beginning of a basement structure (Shipp & Singh 2002). This interpretation allows for a thin, variable thickness, low velocity, sedimentary layer to be present between the base basalt and top of the inferred basement structure. The basalt layer itself appears to contain internal structure, perhaps indicative of thin individual basalt flows separated by low-velocity layers, such as weathered horizons or thin sediment layers.

Fig. 7 shows a typical CMP supergather of the data, six individual CMP ensembles were combined into supergathers in order to reduce spatial aliasing in the τ–p transformed wavefield, to give a trace spacing of 12.5 m within each CMP gather. The τ–p transform was applied using the algorithm of Korenaga *et al.* (1997). A slowness sampling interval dp= 0.005 s km^{-1} was used, the same

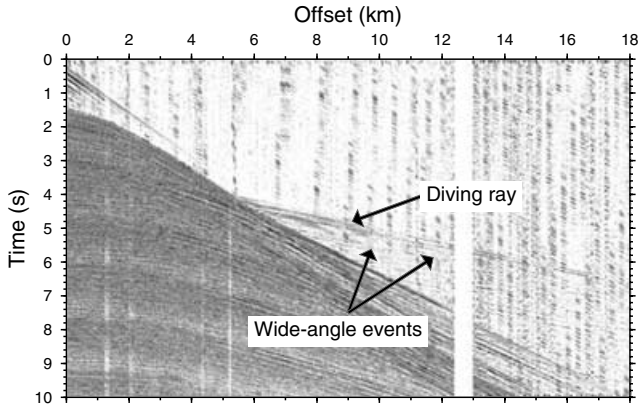

Figure 7. A typical CMP supergather from the Faeroe–Shetland data set after multiple attenuation and amplitude balancing across the data gap at 12–13 km, which corresponds to the offset between the two streamers. The diving ray first arrival can be seen at offsets greater than 5.6 km, with wide-angle reflection events following shortly behind.

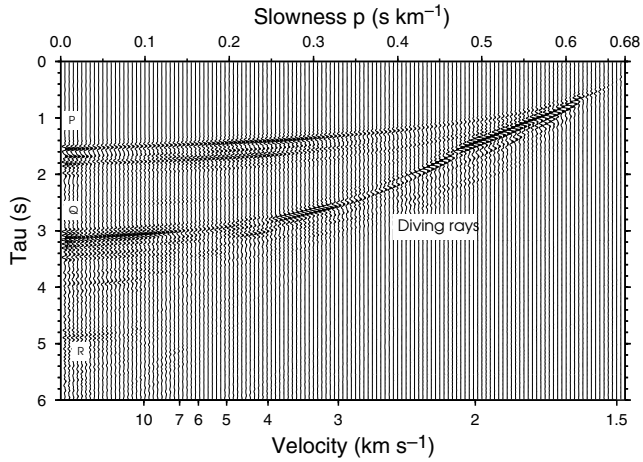

Figure 8. A typical τ–p transformed CMP supergather from the Faeroes–Shetland data after multiple attenuation using hyperbolic Radon filtering, spiking deconvolution and time-variant spectral whitening. P: seafloor reflection ellipse. Q: top basalt reflection ellipse. R: sub-basalt event. The diving ray trajectory from $p = 0.68$–0.20 s km^{-1} is also indicated.

as that used to transform the synthetic data. A typical τ–p transform of a CMP supergather after multiple attenuation is shown in Fig. 8. The strong diving ray trajectory can be seen extending from a high p value across the gather to approximately p= 0.2 s km^{-1} at τ = 2.9 s. This trajectory then merges into the top-basalt reflection ellipse. The seafloor and top basalt reflection ellipses are labelled P and Q, respectively, on Fig. 8. The wide-angle events have extended and strengthened the reflection ellipses in the region of the τ–p wavefield corresponding to low and intermediate values of p as demonstrated with synthetic data in Section 3. This region of the wavefield may include the transformed sub-basalt and basement wide-angle reflection events present in the CMP gather (see Fig. 7). Note that as a result of the Radon filtering the later arrivals (multiples) beneath the diving ray trajectory have been removed.

Although it is possible to use downward continuation to obtain a velocity model at every CMP location, this is computationally expensive and may be unnecessary, in the same way that velocity analyses are not usually carried out at every CMP in conventional

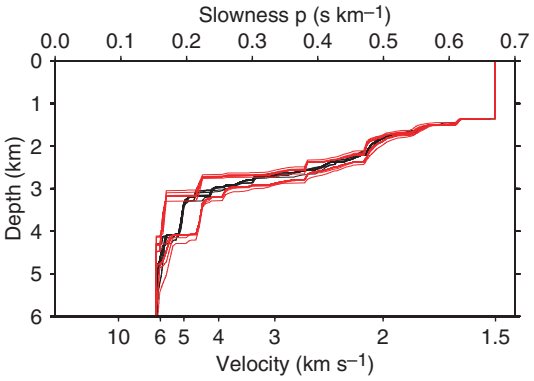

Figure 9. Velocity functions generated using velocity update for 30 iterations from a typical CMP gather (see text for details of method). After a few iterations, the velocity functions determined from the maximum amplitude (red) remain stable in a bimodal distribution. The average velocity functions calculated between successive iterations are indicated in black. A steady state average function (less than 5 per cent change between iterations) was obtained after 11 iterations.

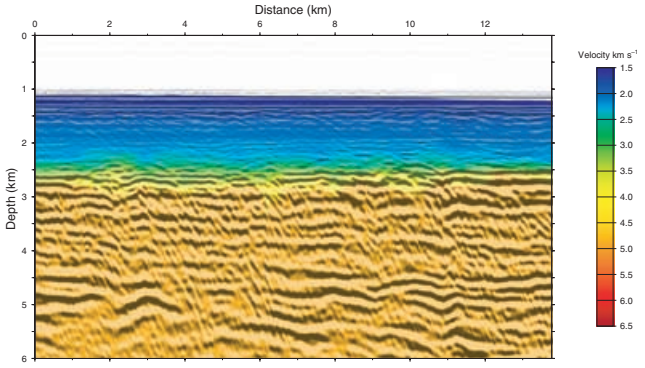

Figure 10. Image of a section of the Faeroe–Shetland data produced with the iteratively determined velocity model with velocities beneath 2.8 km flooded with 4.8 km s^{-1}. The top basalt reflection image at around 2.6 km depth coincides with a large velocity discontinuity at the same depth.

processing. In this exploratory application the selected portion of the line was broken into subsections of thirty CMP gathers, and a velocity model extracted at the end points of each subsection. Velocity functions for the intermediate CMP gathers were determined by linear horizontal interpolation between the two end functions. This end function spacing allows a velocity model to be constructed quickly, and it can easily be revised in the light of initial results. Starting models were obtained using the τ-sum technique (Diebold & Stoffa 1981). Downward continuation was carried out using the iterative method of Clayton & McMechan (1981). As described in Jones *et al.* (2003), successive iterations stabilize in a bimodal range of velocity functions, and the average of the two is used to process the data (Fig. 9). The criterion for the stability of the downward continuation was a less than 5 per cent change in the average function between iterations, which generally happened after about 10 iterations. A slowness cut-off value of $p = 0.16$ s km^{-1} was set, corresponding to a maximum velocity of 6.25 km s^{-1}, in order to allow a search to be performed far enough across the z–p wavefield to detect a diving wave signal associated with the basalt layer, while preventing a velocity over-estimate as the method becomes unreliable in the deeper section. In practice it was not possible to extract the function reliably far into the basalt layer and the section beneath a depth of 2.8 km was flooded with a velocity of 4.8 km s^{-1}, corresponding to the basalt velocity extracted at this depth.

Uncertainty in the velocity function may adversely affect the final image trace in two ways. Firstly, a small moveout in the otherwise horizontal events may occur at high slowness values in the z–p wavefield. Stacking these moved out traces may result in a final image trace that is smeared vertically in depth. Secondly, the position of the event in depth will have an error associated with the velocity function uncertainty. The envelope of possible velocity functions may provide an estimate of the depth uncertainty for individual events.

Fig. 10 shows the stacked seismic image. The seabed can be seen at 1.1 km depth. Beneath this is a 1.5 km layer of relatively undeformed sediments. A strong reflection can be seen extending across the section at about 2.5 km depth coinciding with a velocity discontinuity from about 3.4 to 4.0 km s^{-1}: this is interpreted as the top basalt reflection. Beneath the top basalt interpretation is more difficult because the velocity model used to downward continue the τ–p gather was less well determined at these depths and a constant velocity was used. There appear to be a number of coherent events extending across the section within the sub-basalt region which may be related to the structures within and below the basalt: note that the use of the flooding velocity may have placed reflectors at the wrong depth and degraded the image slightly. The change in the character of the event at 4.5 km depth may correspond to the base of the basalt. Between depths of 4.8 km on the left hand side to 5.5 km on the right hand side a dipping event may indicate the top of the basement. However, if we accept the earlier interpretation (Shipp & Singh 2002) of a low-velocity zone between the basalt and the basement, the depth to these events is incorrect in Fig. 10 because a high (basalt) velocity has been used from approximately 2.8 km depth downwards.

This final velocity image may be compared qualitatively with the conventionally stacked time section of the same data shown in Fig. 6. The rugose top basalt reflector and internal basalt events seen on the Veritas stacked section are also present in the velocity image. Although the velocity model for the final image beneath the basalt is homogenous there are close similarities with the Veritas stack. The high-amplitude events initially interpreted as the base of the basalt in Fig. 6 appear on the final image of Fig. 10 at approximately 5 km depth, and the dipping feature at 5.5–6.0 km depth and 6–14 km distance is thought to be top basement. A refined or better constrained velocity model will reposition these events in depth, and their amplitude may also change. However, the final velocity model has imaged a number of identifiable features that are consistent with Fig. 6 and are, therefore, regarded as real geological features rather than artefacts or random noise generated by the τ–p transformation or by the downward continuation and stacking process.

The velocity model produced by Shipp & Singh (2002) using wavefield inversion is shown in Fig. 11. The inversion was performed to approximately 4 km depth. Beneath the seafloor and sedimentary layer the strong velocity discontinuity corresponding to the top of the basalt layer can be seen at approximately 2.6 km depth. Within the basalt layer there is a degree of velocity variation with a horizontally banded appearance.

In order to compare the velocity variations seen in the images obtained using these two completely independent methods the velocity function obtained from waveform inversion at 8.25 km distance along the profile was used as a downward continuation velocity function for the same gather in the τ–p domain. Fig. 12 shows the z–p wavefield resulting from downward continuation to 4 km depth with this velocity function and a stack of this gather, extrapolated to

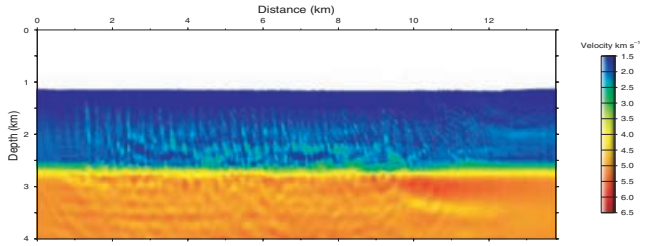

Figure 11. Velocity model from full wavefield inversion for the same section as shown in Fig. 10, after Shipp & Singh (2002). The velocity variations in the basalt layer shown in the waveform inversion result may correspond to images in the basalt layer seen in Fig. 10. Note that the scales are the same but that Fig. 10 extends to greater depth.

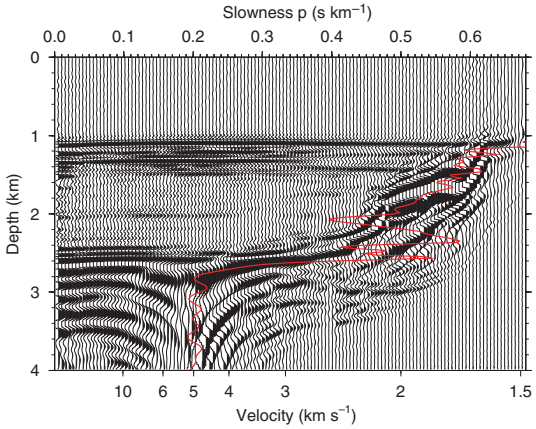

Figure 12. *z–p* wavefield after downward continuation with the coincident velocity function from full waveform inversion (Shipp & Singh 2002) at 8.25 km distance along the profile (see Fig. 11), which is superimposed in red. Note how the independently derived velocity function tracks the high-amplitude turning ray trajectory.

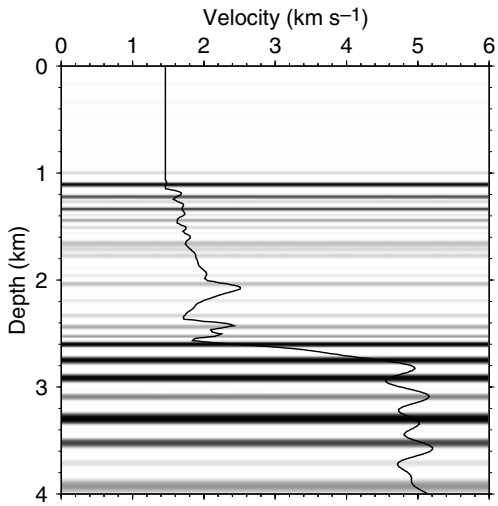

Figure 13. Stack of *z–p* wavefield shown in Fig. 12, extrapolated to form a 1-D image. The structural features in the sediments (1.1–2.6 km depth) and basalt layer (greater than 2.6 km depth) correspond well with the velocity variations predicted from full waveform inversion, shown by the solid curve.

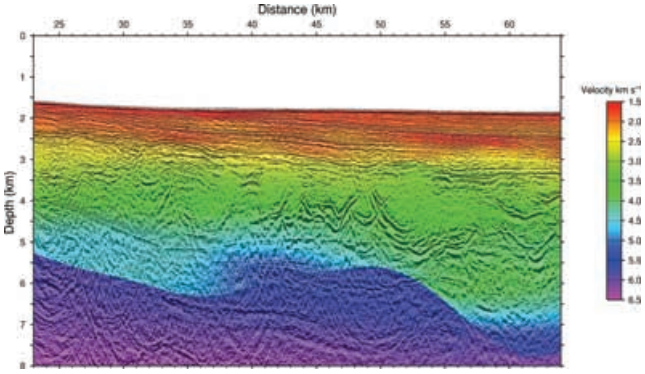

Figure 14. Tomographic inversion velocity model overlain with the depth migrated section obtained from conventional processing, after Bosch *et al.* (2005). Note the multiples that cross the section from 4–5 km downwards. The velocity model correlates well with the structures in the upper 3 km of the profile. The high-amplitude features at about 4 km depth in the centre of the profile are interpreted as the sill complex. The sharp undulating velocity discontinuity at depth may be associated with the basement structure. However, on this profile it is difficult to correlate this basement velocity discontinuity with any coherent seismic events.

form a 1-D image, with the velocity-depth function superimposed, is shown in Fig. 13. These figures show that the waveform inversion-derived velocity function shows short wavelength fluctuations for approximately 0.5 km beneath the seafloor. The wavelength of these fluctuations appears similar to the wavelength of the image trace at this shallow depth. The velocity function variations through the basalt layer also show some correlation with the horizontal events that comprise the internal structure of the layer (Fig. 13).

4.2 Example 2: Thin discontinuous basalt sills

The method was applied to a second marine multichannel seismic data set from the northeast Atlantic margin; this data was collected in the Rockall Trough. The aim here was to produce images of deep events including the basement below a series of basalt sills. The approach differs from the previous section, where a velocity model was obtained from the *z–p* wavefield, in that a pre-existing velocity model was used to produce the images. A comparison is made between the results obtained using the new imaging approach and the results obtained from conventional depth migration using the same velocity model, enabling a direct correlation to be made between the individual events observed on the two sections.

The velocity model was generated during a separate investigation of the same data set by Bosch *et al.* (2005), who selected several arrival phases at both long and short offsets for picking prior to inversion using the JIVE3D traveltime inversion algorithm of Hobro *et al.* (2003). The velocity model was defined by reflections from the top of the sills and diving rays above and below the sills. The velocity model obtained from this inversion, overlain with the corresponding post stack depth-migrated section (Bosch *et al.* 2005), is shown in Fig. 14, for comparison with the profiles produced by downward continuation. Unfortunately, due to time constraints, this section was produced complete with multiple arrivals, which can be seen clearly in the lower part of Fig. 14.

Fifteen km of offset was used in this study, although the data were recorded to 30 km offset using multiple-pass two-ship acquisition (Buhl *et al.* 1982): this offset includes the reflected energy from deeper events, while allowing the τ–p transform to be performed at a reasonable computation cost. The data were reorganized into CMP supergathers with a trace spacing of 25 m. CMP spacing was 50 m, with a total profile length of 40.55 km. The portion of the profile

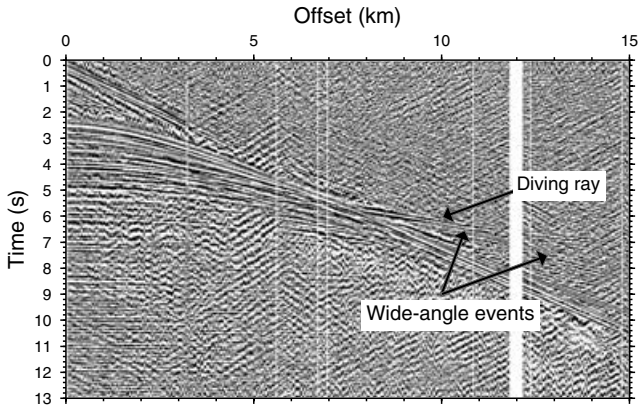

Figure 15. A typical CMP supergather from the Rockall Trough data set after application of a Radon filter to attenuate the seafloor multiple. The first arrival diving ray and some wide-angle reflection events are labelled.

studied here represents about half of the total length of the available data. A typical CMP supergather used for imaging is shown in Fig. 15. A similar multiple removal strategy to that implemented on the Faeroe–Shetland Basin data was applied to this data set. The seafloor multiple was reduced by the application of a Radon filter. Ensemble deconvolution was also applied, enhanced with time variant spectral whitening. The τ–p transform (Korenaga *et al.* 1997) was performed to 13 s TWT for each CMP supergather with a slowness interval (p) of 0.005 s km^{-1}.

The result of a typical τ–p transform is shown in Fig. 16(a). The seafloor reflection ellipse intersects the τ axis at 2.4 s. Other reflection events appear at $\tau = 4$–10 s. The inclusion of the wide-angle arrivals (Fig. 15) enhances the τ–p wavefield reflection ellipses compared with using the shorter offsets alone (see Section 3).

Each τ–p transformed CMP supergather along the line was downward continued using the coincident velocity function from the tomographic inversion velocity model and the result imaged by muting with the velocity function and stacking to give one trace per CMP. Downward continuation was carried out at depth increments of 5 m. A typical z–p wavefield used to form an image trace is shown in Fig. 16(b), prior to mute. The horizontal alignment of the events at 2–4 km depth gives confidence in the velocity model in the upper part of the section. Further down the wavefield at 4–10 km depth some of the events are less horizontal and the wavefield is less ordered. The subhorizontal nature of the events would provide justification for modifying the velocity model at depth in order to improve this horizontal alignment.

In the analysis of this data set, where we are particularly concerned with imaging deep events, it is interesting to examine the extent to which the wide-angle reflection events arriving after the diving ray first arrival at longer offsets (see Fig. 15) can be incorporated into the final image, as noted in Section 3 for synthetic data. A further examination of the effect is made on this data set, using the tomographic inversion velocity model (Bosch *et al.* 2005) to examine an individual slowness-depth wavefield.

The approach is similar to that adopted for synthetic data in Section 3.1. τ–p gathers were produced for two ranges of offset (0–3 and 0–15 km) from one CMP, the τ–p wavefields were each downward continued and the final image traces formed. The CMP used in this case was at a distance of 39.5 km along the profile (see Fig. 19), where there are several interesting events including the basalt sill. The CMP was transformed using the first 3 km of offset (Figs 17a and b) and the complete offset range from 0–15 km (Figs 17c and

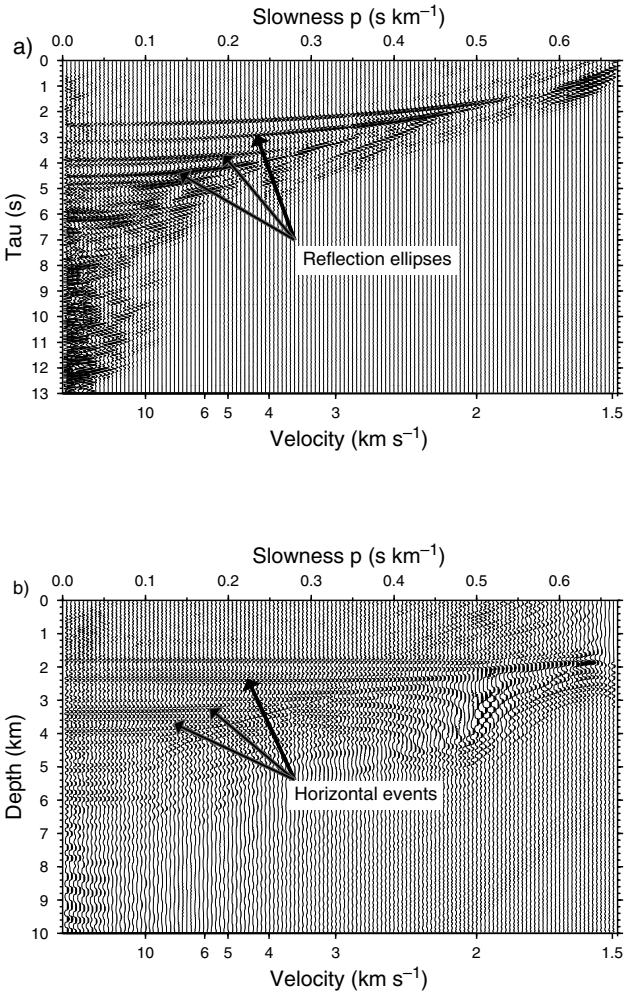

Figure 16. (a) A typical τ–p transformed CMP supergather from the Rockall Trough profile. Three reflection ellipses are indicated with the basement reflection expected at an intercept (τ) time of approximately 7 s (Bosch *et al.* 2005). The effect of the hyperbolic Radon filter attenuating the energy at high to intermediate slownesses is evident in the lower right hand half of the wavefield. (b) Typical z–p wavefield obtained after downward continuation using the tomographic inversion velocity model shown in Fig. 14. The horizontal nature of the events at low to intermediate slowness to a depth of 6 km suggest that the velocity model may be regarded with reasonable confidence. At depths greater than 6 km some of the events appear subhorizontal; modifying the velocity model at these depths might improve the horizontal alignment.

d). The near offset information is clearly visible at low slowness (Fig. 17a). The reflection ellipses have been mapped to horizontal events by downward continuation (Fig. 17b). The 0–15 km transform on the other hand (Fig. 17c) displays the background diving ray trajectory and the reflection ellipses more completely. This wavefield is downward continued in Fig. 17(d) using the same velocity function as used in Fig. 17(b). The horizontal events at depths of 6.0 and 6.8 km extend over a greater range of p values in Fig. 17(d), which will enhance these events when stacked.

The final stacked image traces for the two z–p wavefields of Fig. 17 are presented in Fig. 18. The difference between the 15 and 3 km trace amplitudes is also displayed, showing the contribution to the image trace from the wide-angle data. The wide-angle data has contributed energy mainly at shallow to intermediate depth corresponding to the position of the major horizons within the

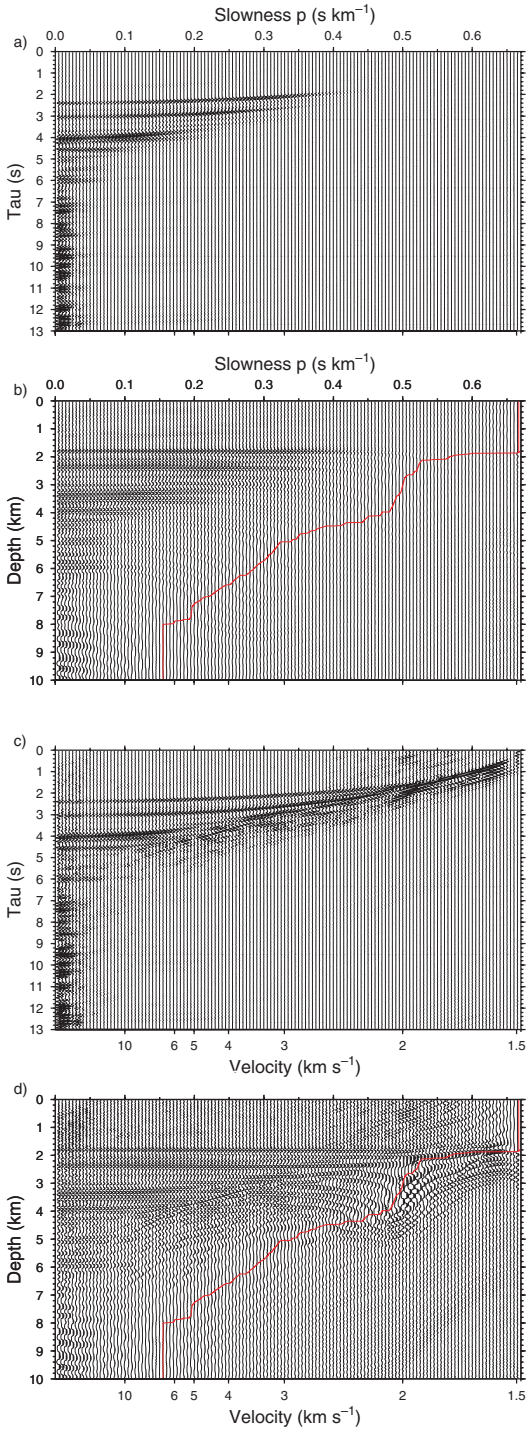

Figure 17. The τ–p and z–p wavefields for a typical CMP supergather of the Rockall Trough data. (a) τ–p wavefield using the first 3 km of the gather. (b) z–p wavefield after downward continuation using the coincident velocity function from the model of Bosch *et al.* (2005) (red line). (c) τ–p wavefield for 15 km of offset. Some extension of the τ–p ellipses relative to the 0–3 km data is evident at $\tau = 6.0$ s. (d) z–p wavefield after downward continuation using the same velocity function as in (b) (red line). Mapping the extended ellipses from (c) to the z–p domain in d) leads to an enhanced image trace after stacking (see Fig. 18).

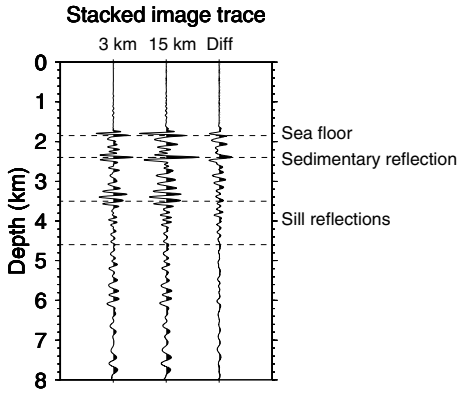

Figure 18. (a) The stacked image traces of Fig. 17(b) and (d) at offset ranges 0–3 and 0–15 km, and the difference between them. The amplitudes of the traces are comparable because the same velocity function was used to mute both slowness-depth wavefields. The inclusion of the longer offset data in the τ–p transform has led to an increase in the amplitude of the 15 km offset final image trace.

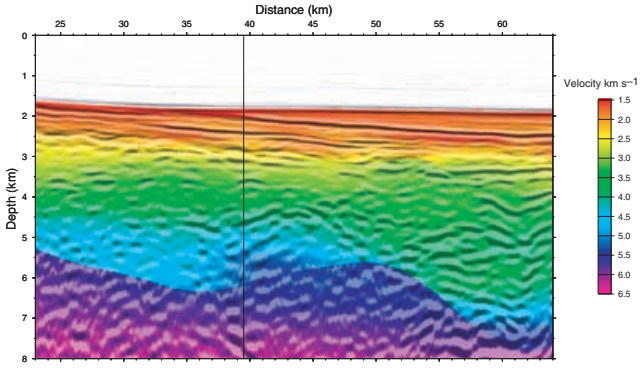

Figure 19. Downward continued stacked section produced using the velocity model from tomographic inversion for comparison with the conventional migrated stack in Fig. 16. The main sedimentary horizons have been recovered and correlate with the variations in the velocity field in the upper 3 km of the profile. The central sill complex has been imaged and a number of diffraction hyperbolae are visible in this part of the profile. At depths greater than 5 km some coherent energy is evident particularly at the bottom right hand corner of the profile. The position of the CMP supergather associated with the z–p wavefield of Figs 18 and 19 is indicated by the black line. The distance scale has been annotated with the same values as Fig. 16.

profile: the two sedimentary layer interfaces and the position of the sill. However, at 6.2 and 7.4 km depth, corresponding to the position of the basement, the difference trace indicates a small but important contribution to the amplitude from the 15 km offset trace.

811 CMP gathers were used to form the final image. The result of downward continuation using the tomographic inversion model along the complete profile is shown in Fig. 19. At shallow depths between the seafloor and approximately 2.5 km sedimentary features and their associated velocity discontinuities have been imaged. Two shallow dipping horizons can be seen with velocities corresponding to that of typical unconsolidated sediments (2.0–2.5 km s^{-1}). Underneath these horizons a more rugose interface is present with a velocity of 2.5 km s^{-1}. The trend of the dip is similar to that of the horizons above and is interpreted as another sedimentary layer. At intermediate depths between 3 and 5 km the velocity field changes slowly and a number of features can be identified within it. The most prominent feature is a high-amplitude event extending across the section, in places laterally discontinuous and undulating. This

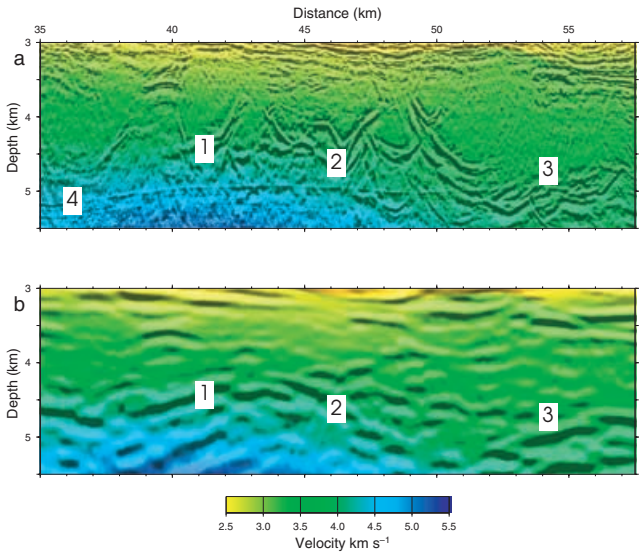

Figure 20. Comparison of images of the sill complex. (a) Conventional depth migrated stack (from Fig. 17), and (b) image stacked in z–p domain after downward continuation. The labels 1, 2 and 3 are in the same position on each panel. Feature 1 can be matched on both images, while events 2 and 3 are more difficult to correlate between the images. However, in (b) discontinuities in the sill complex are more clearly imaged than in (a) where the ends of these disjointed sections are associated with diffraction hyperbolae. A sea bottom multiple is labelled 4 in (a).

feature also generates a number of diffraction hyperbolae indicating the discontinuous nature of the structure, and is interpreted as a minor volcanic intrusion such as a sill, offset in several places. It is also possible to identify features beneath this sill: note coherent structures at 55–62 km offset and 7–8 km depth.

The image of the sill formed from conventional processing and the image produced using our scheme may be compared in detail (Fig. 20). The sill complex can be identified on the complete sections (Figs 14 and 19) at a distance of 35–57 and at 5.0–5.5 km depth. The conventionally processed section (Fig. 20a) shows conspicuous high-amplitude events with high angles of dip and a chaotic character in the middle of the image. At 5.0–5.2 km depth multiples contaminate the section. In the z–p stack (Fig. 20b, there is considerable lateral continuity associated with the event at 35–45 km distance. At distances greater than 45 km the structure appears to bifurcate and becomes generally more disjointed in character. Additionally, several diffraction hyperbolae are associated with this section of the profile. These observations are consistent with either faulting or a stepwise mode of intrusion for the sills. In both cases there would be considerable scattering of energy giving rise to the diffraction hyperbolae observed in this part of the section. Additional features that could be associated with faulting such as vertical offsets in the sedimentary horizons are not observed here and, therefore, a stepwise mode of intrusion is a more plausible explanation for the offsets imaged across the sill, as proposed by Joppen & White (1990).

5 CONCLUSIONS

The objective of the work presented in this paper was the implementation of an imaging scheme capable of exploiting both near and far offset information from long-offset multichannel streamer data. This was achieved by transforming the data from the t–x domain to the τ–p domain. A further transformation to the z–p domain by downward continuation enables a single image trace to be produced for each CMP location by muting the high slowness energy using the velocity function and stacking the remaining low- to intermediate-slowness traces. Application of the downward continuation scheme to synthetic data demonstrated that long-offset events can be used successfully to enhance the final image trace using this method. The velocity function used in the downward continuation may be obtained iteratively from the diving ray trajectory present in the τ–p wavefield after it has been transformed to the z–p domain, or alternatively an independently derived velocity model may be used. The scheme was applied to synthetic data and two marine data sets using offsets of up to 18 km in regions associated with thick sediments interleaved with basalt layers. For both marine data sets, sub-basalt images were obtained and compared with conventionally processed data. Our scheme of processing the reflected and refracted components of the wavefield simultaneously allows the inclusion of information at depth in the final image that is normally discarded during conventional processing.

ACKNOWLEDGMENTS

Veritas DGC Ltd. and the BGS Rockall Consortium kindly made the data sets available. G. Jones was supported by a LITHOS Consortium research studentship.

REFERENCES

Bosch, M., Barton, P., Singh, S.C. & Trinks, I., 2005. Inversion of traveltime data under a statistical model for seismic velocities and layer interfaces, *Geophysics* **70,** 33–43.

Buhl, P., Diebold, J.B. & Stoffa, P.L., 1982. Array length magnification through the use of multiple sources and receiving arrays, *Geophysics,* **47,** 311–315.

Carpenter, M.E., 2001. Seismic imaging using densely sampled, very long offset data, *M. Phil. thesis*, University of Cambridge, UK.

Chapman, C.H., 1981. Generalized radon transforms and slant stacks, *Geophys. J. R. astr. Soc.,* **66,** 445–454.

Clayton, R.W. & McMechan, G.A., 1981. Inversion of refraction data by wavefield continuation, *Geophysics,* **46,** 860–868.

Diebold, J.B. & Stoffa, P.L., 1981. The traveltime equation, tau-p mapping, and inversion of common midpoint data, *Geophysics,* **52,** 1492–1500.

Hobbs, R.W., 2002. Sub-basalt imaging using low frequencies. *J. Conf. Abs.,* **7,** 152–153.

Hobro, J.W.D., Singh, S.C. & Minshull, T.A., 2003. Three-dimensional tomographic inversion of combined reflection and refraction seismic traveltime data, *Geophys. J. Int.,* **151,** 79–93.

Hughes, S., Barton, P.J. & Harrison, D., 1997. Characterizing the Mid-Faeroe Ridge using seismic velocity measurements, *J. geophys. Res.,* **102,** 7837–7847.

Joppen, M. & White, R.S., 1990. The structure and subsidence of Rockall Trough from two-ship seismic experiments, *J. geophys. Res.,* **95,** 19 821–19 837.

Jones, G.D., Barton, P.J. & Singh, S.C., 2003. Combined structure and velocity stacks via the tau-p transform, *Geophys. Prospect.,* **51,** 205–213.

Korenaga, J., Holbrook, W.S., Singh, S.C. & Minshull, T.A., 1997. Natural gas hydrates on the southeast U.S. margin: constraints from full waveform and travel time inversions of wide-angle seismic data, *J. geophys. Res.,* **102,** 15 345–15 365.

Schultz, P.S. & Claerbout, J.F., 1978. Velocity estimation and downward continuation by wavefront synthesis, *Geophysics,* **122,** 837–857.

Shah, P.M. & Levin, F.K., 1973. Gross properties of time distance curves, *Geophysics,* **38,** 643–656.

Shipp, R.M. & Singh, S.C., 2002. Two-dimensional full-wavefield inversion of wide-aperture marine seismic streamer data, *Geophys. J. Int.,* **151,** 325–344.

Zelt, C.A. & Smith, R.B., 1992. Seismic traveltime inversion for 2-D crustal velocity structure, *Geophys. J. Int.,* **108,** 16–34.